Journal of Cluster Science (2022) 33:773–783
https://doi.org/10.1007/s10876-021-02013-8

ORIGINAL PAPER

# Efficient Photocatalytic and Antimicrobial Behaviour of Zinc Oxide Nanoplates Prepared By Hydrothermal Method

Muhammad Munir Sajid[1,2,3] · Naveed Akhtar Shad[2] · Yasir Javed[4] · Muhammad Shafique[5] · Amir Muhammad Afzal[6] · Sadaf Bashir Khan[7] · Nasir Amin[2] · Muhammad Aamir Hassan[5] · Muhammad Umar Hayat Khan[8] · Tayyaba Tarabi[9] · Haifa Zhai[1,3]

Received: 29 September 2020 / Accepted: 22 January 2021 / Published online: 10 February 2021


## Abstract

In this project, the prime focus was to synthesize zinc oxide nanoplates (ZnO-Nps) by a reliable, simple, and low cost facile hydrothermal method. Zinc acetate was used as major precursors; the synthesis was standardized in a 100 mL autoclave, at 180 °C for 24 h which results in nanoplates with 150–300 nm width and thickness 10–60 nm size and mesoporous nature with a specific surface area 126 $cm^2$ $g^{-1}$. The prepared sample was characterized by X-ray powder diffraction (XRPD), scaning electron microscopy (SEM), transmission electron microscopy (TEM), energy dispersive microscopy (EDS), Fourior transfer infrared (FTIR) spectroscopy, X-ray photo electron microscopy (XPS), Brunauer–Emmett–Teller (BET), Photoluminance (PL), and Electrochemical impedance spectroscopy (EIS) techniques. For application purposes, photocatalytic and antimicrobial activities of ZnO-Nps were studied systematically. The material was made photo-active under visible light irradiation for the degradation of the Methyl orange dye in aqueous media. The antimicrobial activity of ZnO-Nps was checked by time kill method, presented the inhibition of growth against clinical isolates of Methicillin-resistant *Staphylococcus aureus* (*MRSA*) and *Escherichia coli* (*E. coli*) after 24 h. However, 12.5 and 6.25 μg is minimal inhibitory concentration (MIC) and 25 and 12.5 μg minimal bactericidal concentration (MBC) of ZnO-Nps against *MRSA* and *E. coli* respectively.

**Keywords** Advance oxidation · Hydrothermal method · Zinc oxide · Photocatalysis · Antimicrobial activity

✉ Muhammad Munir Sajid
m.munirsajid476@gmail.com

✉ Haifa Zhai
haifazhai@126.com

[1] School of Physics, Henan Normal University, Xinxiang, China

[2] Department of Physics, Government College University Allama Iqbal Road, Faisalabad 38000, Pakistan

[3] College of Materials Science and Engineering, Henan Normal University, Xinxiang, China

[4] Department of Physics, University of Agriculture, Faisalabad 38000, Pakistan

[5] Department of Microbiology, Government College University Allama Iqbal Road, Faisalabad 38000, Pakistan

[6] Department of Electrical and Biological Physics, Kwangwoon University, Seoul 01897, South Korea

[7] The State Key Laboratory for New Ceramics and Fine Processing, School of Materials Science and Engineering, Tsinghua University, Beijing 100084, China

[8] Department Agriculture Research Soil and Water Testing Lab Sahiwal, Pakpattan, Pakistan

[9] Department of Chemistry, Government College Women University, Faisalabad 38000, Pakistan

## Introduction

Mineral water production and degradation of organic impurities in water using the advanced oxidation process (AOP) semiconductor photocatalysts accept the much consideration and are in the front line of central studies and technological approaches in recent years [1, 2]. The industrial wastewater contains a small number of dye molecules, which stimulate water contamination as many pollutants are non-reactive towards light, acids, bases and $O_2$, thus, the colour of the material turns permanent. Dye degradation comprises action in which the macroscopic dye molecule is split up into lower molecules like carbon dioxide and purified by-products [3, 4]. From many methods for water remediation, reported adsorption, coagulation, filtration [5] and photocatalysis [6], the latter technique is an exceptionally favourable route for water cleaning from harmful contaminants owing to the simplicity of equipment and complete degradation of pollutants [7].

Photocatalysis represents an advanced oxidation process (AOP) in which the interaction of light to a semiconducting material normally metallic elemental oxides, which give electron–hole pairs (ehp) and leads to successful proceeding of electrons from valence band to conduction band [8]. The electron interacts with $O_2$ and hole with $H_2O$ molecules to form superoxide anions and $^{\cdot}OH$ radical, which is highly reducing and oxidizing agent for the organic dye compounds used in many industries [9]. The primary mechanism of AOP is to increase the adsorption capacity of semiconductor material towards organic contaminants through using low consumption source such as in visible light [10, 11].

Zinc Oxide (ZnO) nanomaterials have been studied extensively in the past years and presented unique properties for multidisciplinary applications such as sensors [12], catalyst [13], high effective and functional devices [14] and photoelectron devices [15, 16]. ZnO has a wide direct energy bandgap (3.1–3.4 eV) semiconductor at ambient conditions [17]. ZnO materials with different nanostructured are utilized for photocatalytic, photochemical, optoelectronic and electrical applications [6, 18]. However, the photocatalytic application of native ZnO has been constructed to the UV spectrum of light attributable to the broad bandgap. Since ultraviolet illumination just accounts for 5% of the solar spectrum, besides, its stableness and fast recombination of charge carriers ($ehp_s$) under illumination are receded that are necessary to be addressed [19, 20].

Likewise, the interaction between bacteria and nanomaterials surface is a versatile tool to access the antibacterial activity of the materials. Till date, different ZnO nanostructures such as one-dimensional, two-dimensional, spherical, and hierarchical nanostructures have been prepared and utilized for photocatalytic degradation of organic pollutants and drug-resistant bacteria. The advantage of ZnO nanomaterial usage as antibacterial purposes is that they can be promptly blended with wound dressing stuff. So this study is an attempt to enhance the photocatalytic and antimicrobial activity of the ZnO-Nps.

Synthesis of ZnO nanomaterials have been reported in literature using different protocols such as combustion method [21, 22], thermal decomposition [23], sol–gel method [24], hydrothermal method [25], Laser ablation [26], electrochemical [27], ultrasound [28], microwave-assisted method [29], co-precipitation method [30, 31], two-step mecheno-chemical thermal synthesis [32], biological methods [33–37] and electrophoretic deposition [38]. Among these different methods, the hydrothermal method is a versatile synthesis method and favourable than many other synthesis processes, imputable energy reduction, low handling temperatures, more crystallinity, controlled growth, the adeptness to recycle wastes, the secure and appropriate disposal of rubbishes [39, 40]. Therefore, we used hydrothermal method for the synthesis of ZnO catalyst.

From the literature survey [2, 4, 41–47] and previous discussion, we have come to know that for photocatalytic and antimicrobial purposes the catalyst morphology, the synthesis route, and specific surface area have significant effects. Therefore, stimulated from these concepts, in the present report, ZnO-Nps were prepared, as ZnO with novel nanoplate morphology is rarely reported using a hydrothermal method which gives small grain size with improved crystallinity and larger surface area as compared to other methods. The attractive features of ZnO and its extensive applications motivate scientists to explore further bright aspects of this material. Different properties of the ZnO catalyst were quantified by XRPD, XPS, SEM, TEM, EDS, FT-IR, BET, PL, and EIS. The photocatalytic activity of ZnO-Nps photocatalyst was inquired by the degradation of Methylene orange (MO) dye under visible light. Antimicrobial properties of the ZnO-Nps were also investigated. This work reveals the potential of ZnO nanopalates for environmental remediation as well as in Antimicrobial effect.

## Materials and Methods

Zinc acetate, cetyl trimethyl ammonium bromide (CTAB), and MO were purchased from Merck Company. In all tests double distilled water was used. In a typical procedure, 6.30 g zinc acetate [$Zn(CH_3COO)_2{\cdot}2H_2O$] and 0.70 g CTAB was dissolved in 70 mL deionized water,

respectively under vigorous stirring for 2 h. Hydrochloric acid (HCl) and sodium hydroxide (NaOH) were exploited to adjust the pH value of solution around eight as and if required. The solution so formed was transferred into 100 mL Teflon lined autoclave. The autoclave was kept in the oven at 180 °C for 24 h. Subsequently, the autoclave was cooled to room temperature naturally. The obtained precipitates were filtered, washed several times with deionized water and ethanol alternatively and dried at 60 °C in oven for 8 h [48, 49]. The as-synthesized ZnO sample was then characterized for different physical and chemical conformations, i.e., X-ray powder diffraction, SEM, TEM, EDX, XPS, FTIR spectroscopy, EIS, BET surface area analysis and photoluminescence techniques. The proposed mechanism digram for the synthesis of ZnO-Nps by hydrothermal method is illustrated in Fig. 1.

## Photocatalytic Activity

The photocatalytic activity of the ZnO photocatalyst was investigated over the Methylene orange (MO) dye under the visible light. A Xenon lamp with accumulative 300 W was used as a visible light source. A Perkin Elmer λ 35 UV–Vis spectrophotometer is used to notify the absorbance spectra of the solution. For experimentations, 100 mg of the ZnO catalyst was first dispersed to 100 mL of an aqueous solution containing 100 mg MO dye. The aqueous solution was stirred vigorously for 2 h in the dark to reach adsorption–desorption equilibrium between MO dye and ZnO catalyst. To avoid any thermal degradation of MO in solution, an ice bath was used throughout the experimentation and constant stirring was maintained. After appropriate sessions of irradiation, a small amount of samples ~ 3 mL suspensions were periodically removed after each 30 min and centrifuged at 5000 rpm and tested for the residual concentration of MO in the solution which has a maximum absorbance at a maximum wavelength of 464 nm [50, 51]. The degradation efficiency is calculated by following the equation;

$$\text{Degradation efficiency} = (C_0 - C_t)/C_0 \quad (1)$$

where $C_0$ is the initial concentration of dye at adsorption–desorption equilibrium, while $C_t$ is the concentration at a later time 't' [52, 53].

## Antimicrobial Activity

The antibacterial activity of ZnO-Nps was identified by time kill method against clinical isolates of Methicillin-resistant *Staphylococcus aureus* (*MRSA*) and *Escherichia coli* (*E. coli*). In time kill method, optical density (OD) of bacterial culture (*MRSA* and *E. coli*) containg ZnO-Nps was recored after different interval of time [54]. There were 100 µg ZnO-Nps added into 3 mL of LB broth with 100 µL of each bacteria inoculum prepared with McFarland concentration inubated along with positive control containing no ZnO-Nps for comparison. The optical

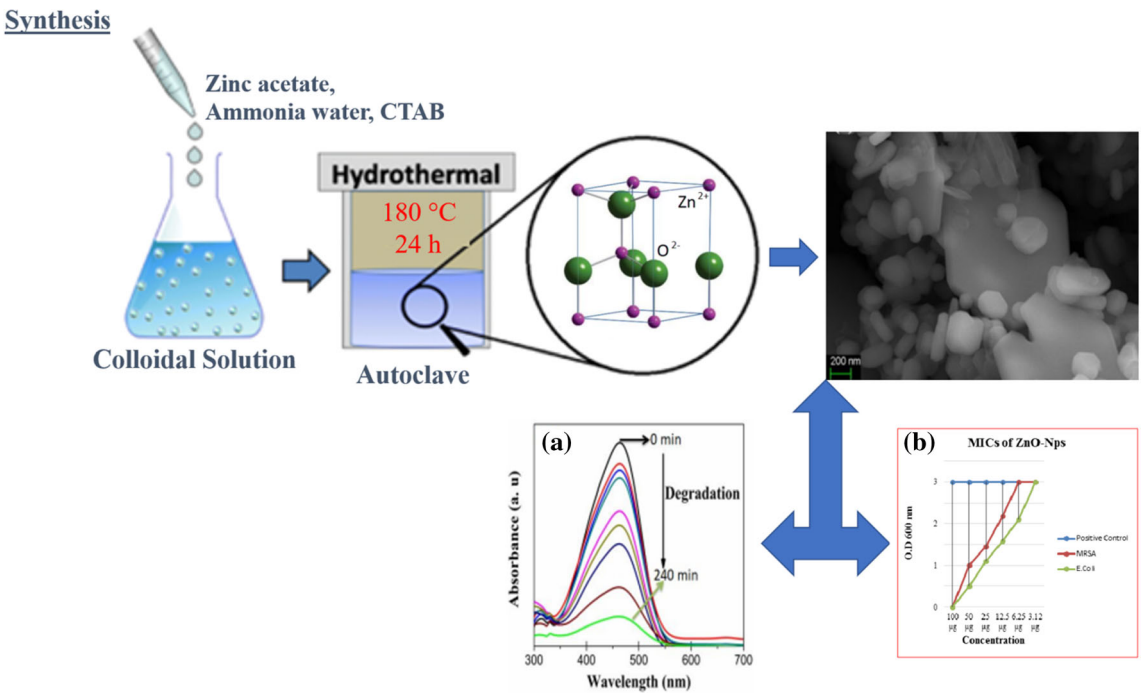


**Fig. 1** Schematic illustration of the proposed hydrothermal synthesis of ZnO-Nps and its application

density was checked after different intervals of time (2, 4, 8, 21 and 24 h) [55].

The minimal inhibitory concentration (MIC) was identified by micro-dilution method, including 100 µL of LB broth added in each well of micro-titration plates with 10 µL of each bacterial strains with twofold dilution of ZnO-Nps (100, 50, 25, 12.5, 6.25 and 3.125 µg) and recorded O.D600 after the incubation at 37 °C for 16–20 h [56]. For identification of ZnO-Nps are bactericidal or bacteriostatic, minimal bactericidal concentration (MBC) was used, 10 µL of culture form each well of MICs finding and grown LB agar medium by the incubation at 37 °C for overnight [57].

## Results and Discussion

For phase purity and crystallinity, the ZnO nano powder was characterized by XRPD technique as illustrated in Fig. 2. The sharp peaks indicating intense crystal quality of ZnO with the sharpest peak positioned at 38.39°. All the peaks are indexed with JCPDS card No. 01-076-0704 with a lattice parameter of a = 0.325 nm and c = 0.521 nm and well-matched from the previously reported results [58, 59]. It can be seen from Fig. 2 that no other phase of ZnO is present, consequently confirms the purity of the output product.

For morphology and topographical purposes, SEM characterization was used and the micrographs of as-synthesized ZnO are shown in Fig. 3a–c. The SEM images were taken at high magnification, indicating the plate type morphology with width 150–300 nm and thickness 10–60 nm estimated using ImageJ software. It is revealed, the formation of Nps is owed to chelation of metal cations in the suspension [47], which is also confirmed by TEM analysis (Fig. 3e). A plate-like morphology indicates the feasibility of formed nanostructures for the photocatalytic application. Although it is difficult to take the idea about the particle thickness in TEM image porous surfaces can be witnessed. To confirm the chemical composition of the as-synthesized sample, the Energy-dispersive X-ray spectroscopic (EDX) technique was applied, the result of EDX indicate that the sample is composed of Zn and O elements, no other impurity or contamination was noticed within the detection limit, the C and Pt peaks are raised due to background carbon tape and Pt coating as displayed in Fig. 3d [59, 60].

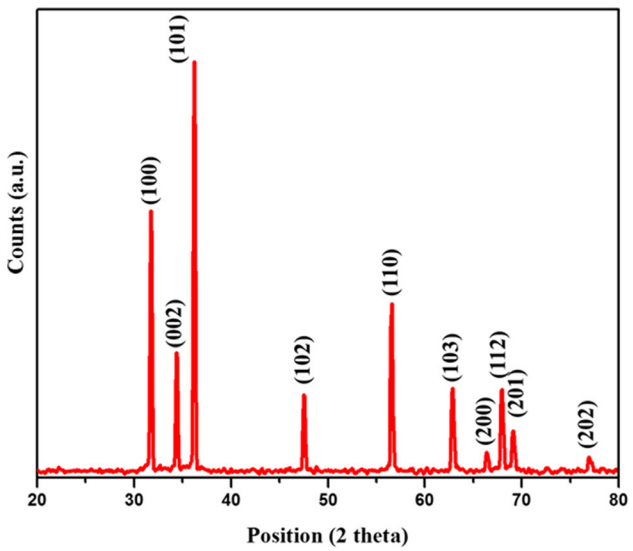


**Fig. 2** The XRD pattern for the as-synthesized ZnO-Nps by hydrothermal method

ZnO Nps have been further characterized by X-ray photoelectron spectroscopy (XPS) to probe chemical composition, as XPS is a flexible tool for the chemical conformation investigation and surface state purity of the samples, Fig. 4 is showing the XPS results which confirmed that the as-synthesized material is composed of pure Zn and O elements. The binding energies of Zn for core levels 2p are 1027.40 eV for $2p_{3/2}$ and 1014.14 eV for $2p_{1/2}$ as shown in high resolution XPS spectra (Fig. 4, inset) and for O core levels 2s, the typical binding energy 530.4 eV is noticed [60, 61]. The FTIR spectroscopy of ZnO Nps provides information about the attached functional groups (Fig. 5). The absorbance from 400 to 480 $cm^{-1}$ is owed to Zn–O stretching mode, the peak at 1630 $cm^{-1}$ is indicating O–H bending band and the broadband at 3480 $cm^{-1}$ is the O–H stretching mode indicating the absorbance of water at the ZnO-Nps surface [61, 62]. Thus, the FTIR result is also confirming the formation of pure ZnO catalyst. XRD, EDX, XPS, and FTIR results confirm that the product is pure ZnO.

It is well known that photocatalytic phenomena are surface area dependent, higher the surface area, greater will be the absorption and consequently raise the degradation of the pollutants. The specific Brunauer–Emmett–Teller (BET) surface area of the ZnO-Nps was evaluated by adsorption–desorption isotherms of nitrogen gas in the pressure range 0.05–1 (Fig. 6). The BET area was found 126 $cm^2\ g^{-1}$ which is sufficiently large and indicating high crystalline nature and regular placement of pores within the structures. The pore range ensued by Barret–Joyner–Halender (BJH) method and was found the average pore size of 10 nm (Fig. 6, inset). The pore size intense peak distribution is mostly from 3 to 9 nm indicating the nanoporous within the ZnO-Nps. This type of nanostructures is considered well suited for photocatalysis as it provides effective cites for reactants and products. The ZnO-Nps isotherm followed a typical type III isotherm presenting the

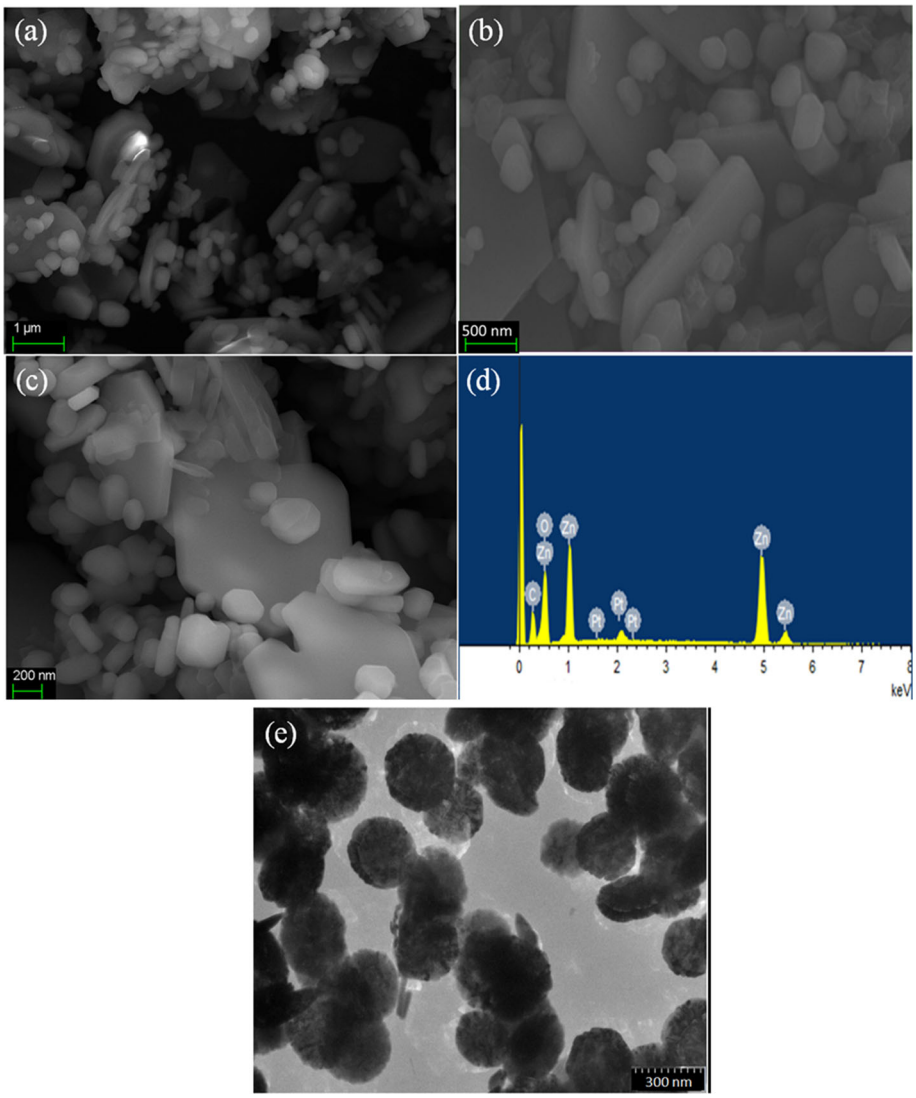


**Fig. 3** SEM image at **a** low magnification, and **b**, **c** high magnification, **d** EDX spectra of as-synthesised ZnO-Nps, **e** TEM image of ZnO-Nps synthesized hydrothermally at 180 °C

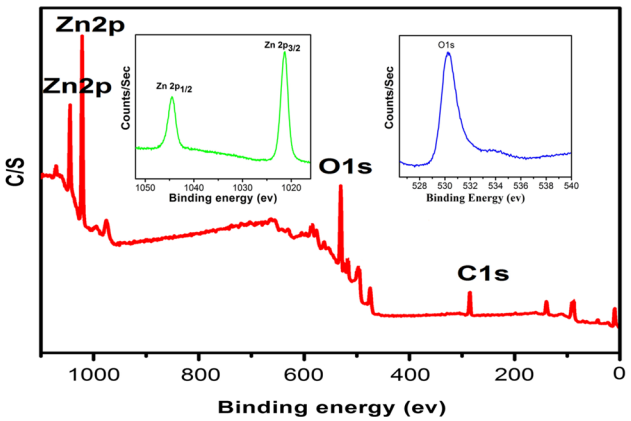


**Fig. 4** Wide scan total XPS spectrum of the ZnO-Nps photocatalyst, (inset) High resolution spectra of Zn 2p and O 1s

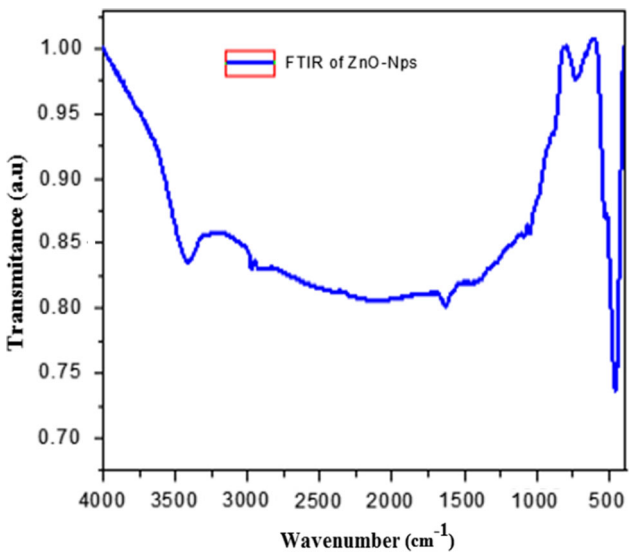


**Fig. 5** FTIR spectra of hydrothermally synthesized ZnO nanoplates

hysteresis of $H_3$ type indicate the formation of wide frame group of atoms and reveal the presence of mesopores within the structure and strong adsorbate–adsorbate

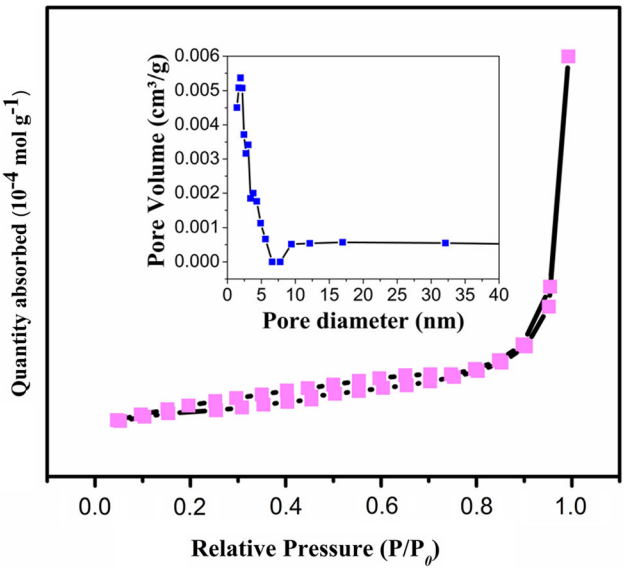


**Fig. 6** $N_2$ absorption–desorption curve for BET surface area measurements of ZnO-Nps

interaction [63, 64]. So, it is confirming that ZnO-Nps is highly crystalline mesoporous material.

PL spectrum for ZnO-Nps in Fig. 7a depicts a strong broad emission band in visible-range. This emission is indicating the potential of ZnO-Nps in the visible light region; it means that visible PL bands correspond to a deep level in ZnO-Nps that can be excited by the visible light source. From photocatalytic degradation point of view, this particular behaviour to absorb visible light is very promising for the photocatalysis process. The Photoluminance (PL) result is matching inconsistent with the previously reported results [65, 66]. Electrochemical impedance spectroscopy (EIS) provides a versatile method for the psychoanalysis of the electron transfer, conduction, and surface area of materials. Figure 7b exhibits the comparability of the bare electrode and modified ZnO GCE graphical record in 0.1 M of $LiSO_4$ solution. The spectrum of the ZnO GCE is indicated by a semicircle at the higher frequency and represents nearly a straight line at low frequency. The results exhibit that the ZnO GCE is an electron channel moderated at high frequency and diffusion operated at low frequencies. The final result shows that the ZnO GCE brings down the electron transportation impedance and turn into controlled electron transmits activity, suggesting a significantly minimized recombination rate.

## Photocatalytic Analysis of Zno-Nps Prepared By Hydrothermal Method

For a photocatalytic response, ZnO-Nps were used for the degradation of MO dye solution under the visible light irradiation; for comparison, the photocatalytic response without ZnO catalyst just under visible light and ZnO-Nps without visible light were investigated. The absorption spectra of MO dye solution after particular irradiation of visible light intervals over the ZnO-Nps is depicted in Fig. 8a. The typical absorption peak of MO is detected at 464 nm. The strength of the absorption peak decreased noticeably with prolong of the visible irradiation time [67]. MO dye concentration decreases to 0.09 mg $L^{-1}$ upon visible light irradiation for 4 h. The colour of MO dye solution changes from yellow to colourless. The $C/C_0$ ratio from Fig. 8b indicates that the ZnO-Nps conduct ordinal photocatalytic response for MO in the absence of visible light. Similarly, no photocatalytic activity was observed with only visible light illumination. This exhibits that degradation of MO over the ZnO-Nps is light-dependent [68, 69]. The photocatalytic experiment of MO dye solution over the ZnO-Nps was repeated three times and the calculated error-bar for efficiency is shown in Fig. 8c, which also confirm the recyclability and stability of ZnO-Nps photocatalyst. The photocatalytic decomposition process is the absorption of pollutant dye molecules on ZnO-Nps surface. The diffusion of electron–hole charge carriers on the ZnO-Np surface and the photocatalytic reaction is explained in the following equations.

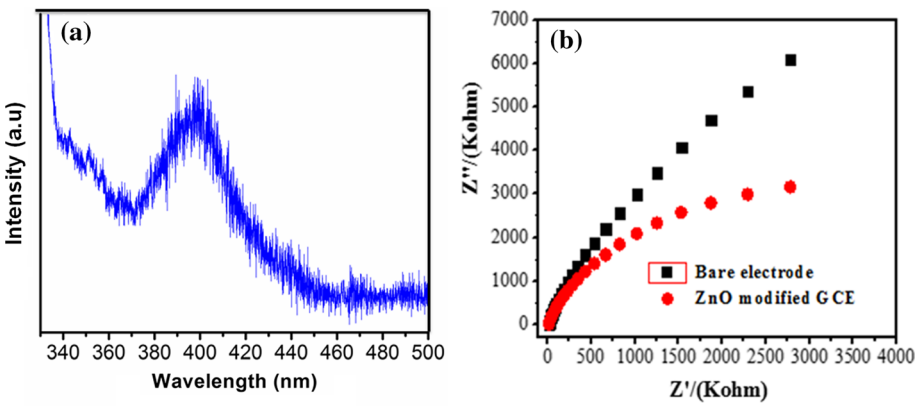


**Fig. 7** **a** Photoluminescence spectra of hydrothermally synthesized ZnO nanoplates, **b** EIS (in Nyquist plots) of modified ZnO GCE in 0.1 M of $LiSO_4$ showed the reduce charge transfer impedance and recombination rate

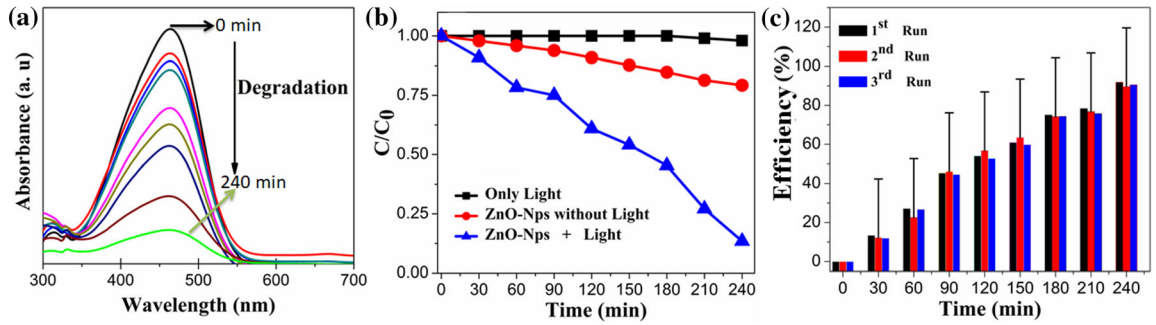


**Fig. 8** **a** Follow up of MO dye solution degradation overtime under visible light using UV–vis spectrophotometer, **b** MO dye concentration with respect to initial concentration for different irradiation time, **c** recyclability for the photocatalytic performance of dye solution for three cycles (error bar shows the stability of the nanomaterials)

$$\text{ZnO-Nps} + h\nu \rightarrow {}^{*}\text{ZnO-Nps}(e^{-} + h^{+}) \quad (2)$$

Photo-oxidation reaction

$$H_2O + h^{+} \rightarrow OH^{-} + H^{+} \quad (3)$$

And photo reduction reaction

$$O_2 + e^{-} \rightarrow O_2^{-} \quad (4)$$

$$O_2^{-} + H^{+} \rightarrow {}^{\cdot}OH \quad (5)$$

Overall reaction

$$OH^{\cdot} + O_2^{-} + H^{+} + \text{MO(dye)} \rightarrow CO_2 + H_2O + \text{Degradation by-products} \quad (6)$$

When a photon of appropriate energy i.e. equal or greater than the energy bandgap of the ZnO-Nps interact at the surface, an electron–hole pair is generated, the electron transfers to the conduction band and interact with the oxygen molecule to make superoxide ion. This ion interacts with a water molecule and creates a series of hydroxyl radical, meanwhile, the positive hole created in the valance band interact with hydrogen ion to create hydroxyl radical [70]. These series of hydroxyl radicals from both sides being a strong and powerful oxidizing agent that degrade the MO dye molecules into the harmless form or minerals as proposed in Eq. (6) [71]. The involved propose mechanism for photocatalytic activity of ZnO-Nps is illustrated in Fig. 9.

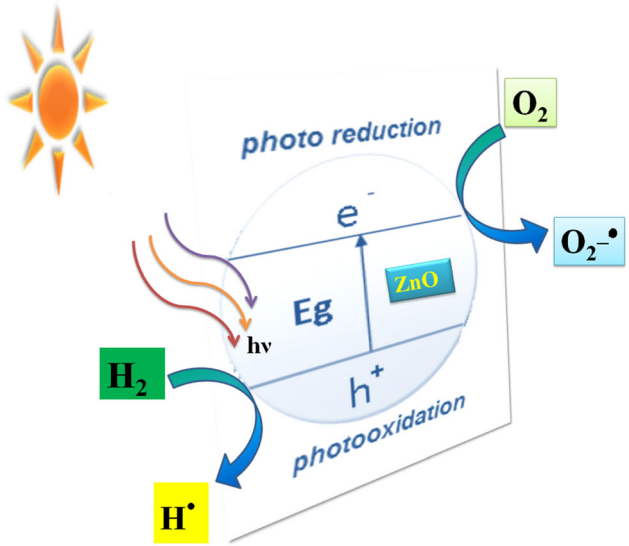


**Fig. 9** Proposed photocatalytic mechanism of the as-synthesized ZnO-Nps by hydrothermal method

## Evaluation of Antimicrobial Activity of ZnO-Nps Prepared By Hydrothermal Method

ZnO is non-toxic, bio-safe and has higher antibacterial potency, used as healing wounds and take advantage as nanomedicine against treating different bacteria and diseases including cancer. It has well established anti-microbial activity as studied by Farzana [72]. An investigation has been made against the effect of ZnO-NPs on the antimicrobial inhibition rate of *MRSA* and *E. coli*. *MRSA* and *E. coli* are harmful bacteria which are commonly found in food, water, intestinal, and throat infection diseases. The exact mechanism of interaction of the ZnO-Nps with bacterial cells is even arguable and unclear. Thus effective and cheap antibacterial agents should be developed to inhibit the bacterial growths.

The analyzed results are obtained at different incubation intervals (24 h) of strains with and without NPs at 37 °C in the incubation chamber. Absorption spectrometer recorded the results at OD of 600 nm for the variation of time of incubation. The bacteria growth curve to time-kill assay has been shown in Fig. 10a, b. Untreated bacterial strains are controls in this experiment. ZnO-NPs have shown antimicrobial effect towards all the strains.

Growth trend of bacteria inhibited by ZnO-Nps has been observed to a significant rate as shown in graphs and inset. The rate of *MRSA* bacteria has been inhibited up to 7.44, 45.10, 82.00, 100.51, and 219.5% for 2, 4, 8, 21 and 24 h of incubation respectively against 265% of bacterial growth at

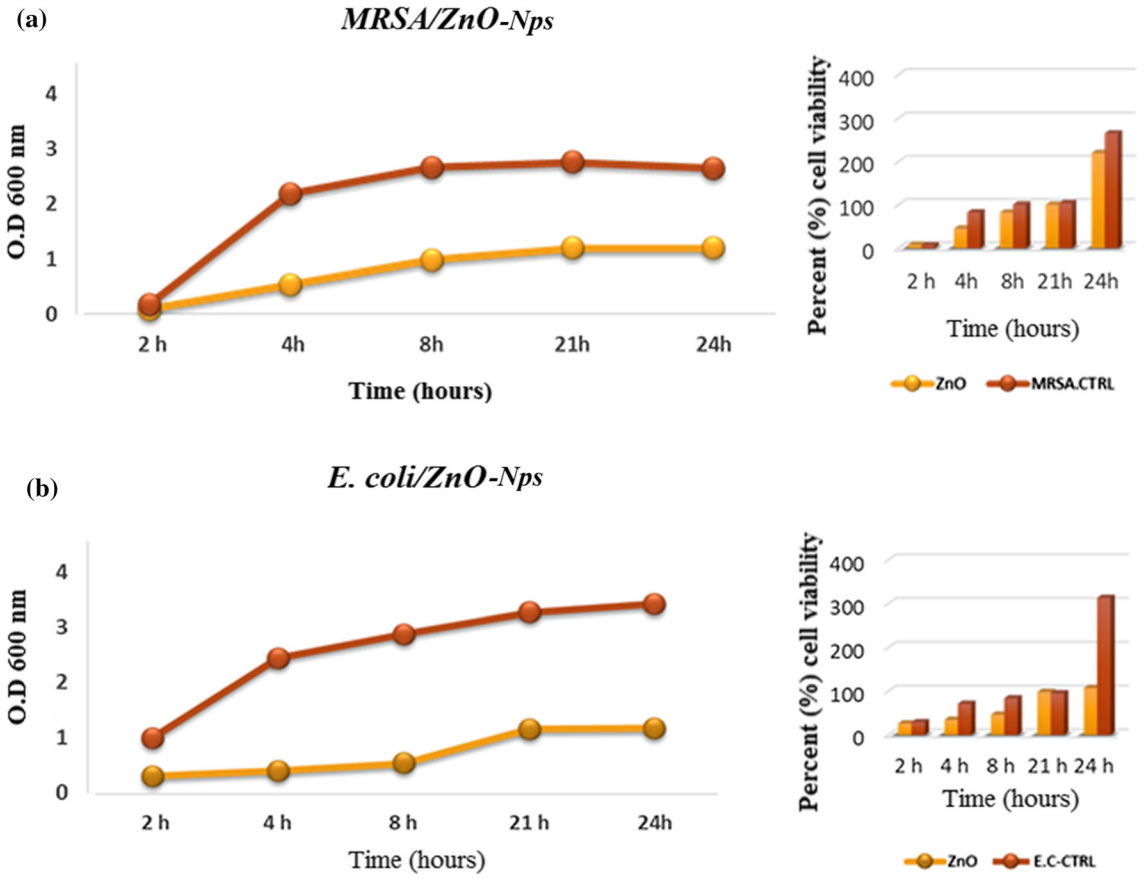


**Fig. 10** Illustration of the effect of **a** ZnO-Nps on *MRSA*, **b** ZnO-Nps on *E. coil* bacterial strains at the various time intervals

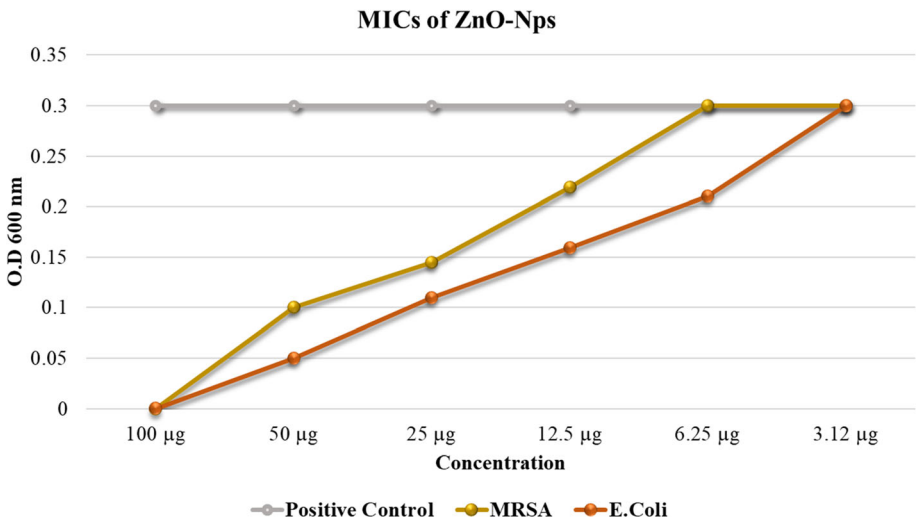


**Fig. 11** MICs of ZnO-NPs against *MRSA* and *E. coli*

24 h, as shown in Fig. 10a. Similarly, Fig. 10b illustrated the rate of *E. coli* has been inhibited by ZnO-NPs up to 26.48, 34.85, 46.56, 98.51, and 107.6% for 2, 4, 8, 21 and 24 h of incubation against 313.3% of bacterial growth at 24 h. Effect of ZnO-Nps on bacterial growth inhibition has been reported by Nicole Jones for antibacterial activity of ZnO nanoparticles [73]. Raghupathi has reported size-dependent bacterial inhibition growth and mechanism of ZnO nanoparticles [74].

There are several theories on the mechanism of loss in cell viability of bacteria. Recent research has provided the reason for charge unbalancing caused by the contact of Nps

with the membrane of the cell (bacteria). Due to electrostatic interaction caused between the positively charged (electron acceptors) ZnO-Nps and negatively charged cell membrane of bacteria resulted in the transfer of charges from bacteria membrane to ZnO-Nps, thus caused the enveloping the cell membrane and inducing the production of reactive oxygen species into the cells. The ZnO-Nps released $Zn^{2+}$ ions, and these positive metal ions of $Zn^{2+}$ penetrate the cells resulting in bacterial cell death [75].

The MICs result revealed that the 12.5 and 6.25 μg of ZnO-NPs are minimal concentration which inhibited the growth of *MRSA* and *E. coli* respectively as shown in Fig. 11. In case of MBCs there is no growth was observed in those plate streaked from MICs well with 25 and 12.5 μg ZnO-Nps against *MRSA* and *E. coli* respectively. *MRSA* and *E. coli* are clinically significant bacteria which are commonly found in food and water also responsible for causing intestinal, and throat infection diseases which lead to bacteremia [76]. Due to evolution in these bacteria, modifying themselves by developing various antibiotics resistance mechanism. Thus effective and cheap antibacterial agents those are alternatives of these antibiotics should be developed to combat these multidrug resistant bacteria. Further studies can be conducted by varying the doses of ZnO-Nps into bacteria and also conjugating it with other therapies and drug for the synergistic effect of treating different clinically significant pathogens.

## Conclusion

In summary, the ZnO-Nps were successfully synthesized by facile hydrothermal method. The XRD, EDX, XPS and FTIR confirm the formation of pure ZnO. The SEM, TEM micrographs of hydrothermally prepared ZnO show the morphology with nanoplates type with 150–300 nm width and thickness 10–60 nm. The ZnO-Nps comprises a sufficiently large surface area 126 $cm^2\ g^{-1}$ and indicating the nanopores within the ZnO-Nps, which enhanced the photocatalysis and antimicrobial activity. The obtained PL results also reveal the ZnO visible activity in the visible regions. These results indicate that the as-synthesized ZnO is a promising candidate for photocatalytic activity as well as in antimicrobial discipline.

**Acknowledgements** Dr. Muhammad Munir Sajid is thankful to Dr. Zhengjun Zhang for supporting characterization techniques and keen interest, Tsinghua University; Beijing, China.

**Funding** This work was financially supported by the State Scholarship Fund of China Scholarship Council (Grant No. 201808410144), the National Natural Science Foundation of China (Grant No. 51202107), and Foundation of Henan Educational Committee (Grant No. 20A480003).

## Compliance with Ethical Standards

**Conflict of Interest** The authors declare that they have no conflict of interest.

## References

1. N. A. Shad, et al. (2019). Photocatalytic degradation performance of cadmium tungstate ($CdWO_4$) nanosheets-assembly and their hydrogen storage features. *Ceram. Int.* **45**, 19015–19021.
2. M. M. Sajid, et al. (2019). Fast Surface charge transfer with reduced band gap energy of $FeVO_4$/graphene nanocomposite and study of its electrochemical property and enhanced photocatalytic activity. *Arab. J. Sci. Eng.* **44**, 6659–6667.
3. Y. Li, X. Xiao, and Z. Ye (2019). Fabrication of $BiVO_4$/RGO/$Ag_3PO_4$ ternary composite photocatalysts with enhanced photocatalytic performance. *Appl. Sur. Sci.* **467**, 902–911.
4. M. M. Sajid, et al. (2018). Visible light assisted photocatalytic degradation of crystal violet dye and electrochemical detection of ascorbic acid using a $BiVO_4$/$FeVO_4$ heterojunction composite. *RSC Adv.* **8** (42), 23489–23498.
5. J. Zhu, et al. (2013). Magnetic nanocomposites for environmental remediation. *Adv. Powder Technol.* **24** (2), 459–467.
6. A. Ashour, et al. (2006). Physical properties of ZnO thin films deposited by spray pyrolysis technique. *App. Sur. Sci.* **252** (22), 7844–7848.
7. L. Zhang, et al. (2012). Efficient removal of methylene blue over composite-phase BiVO4 fabricated by hydrothermal control synthesis. *Mater. Chem. Phys.* **136** (2–3), 897–902.
8. S. G. Babu, et al. (2019). Synergistic effect of sono-photocatalytic process for the degradation of organic pollutants using CuO-$TiO_2$/rGO. *Ultrason. Sonochem.* **50**, 218–223.
9. J. He, et al. (2019). Superoxide/peroxide chemistry extends charge carriers lifetime but undermines chemical stability of $CH_3NH_3PbI_3$ exposed to oxygen: time-domain ab initio analysis. *J. Am. Chem. Soc.* **141** (4), 5798–5807.
10. S. Kumar, et al., Photocatalytic degradation of organic pollutants in water using graphene oxide composite,. A new generation material graphene: applications in water technology. Springer, New York, pp 413–438.
11. M. M. Sajid, et al. (2019). Hydrothermal fabrication of monoclinic bismuth vanadate (m-BiVO4) nanoparticles for photocatalytic degradation of toxic organic dyes. *Mater. Sci. Eng. B* **242**, 83–89.
12. X. Cheng, et al. (2004). ZnO nanoparticulate thin film: preparation, characterization and gas-sensing property. *Sens. Actuators B* **102** (2), 248–252.
13. S. S. Joshi, et al. (2006). Role of ligands in the formation, phase stabilization, structural and magnetic properties of α-$Fe_2O_3$ nanoparticles. *J. Nanopart. Res.* **8** (5), 635–643.
14. Y. Huang, et al. (2006). Controlled synthesis and field emission properties of ZnO nanostructures with different morphologies. *J. Nanosci. Nanotechnol.* **6** (3), 787–790.
15. S. Y. Lee, et al. (2005). Fabrication of ZnO thin film diode using laser annealing. *Thin Solid Films* **473** (1), 31–34.
16. Z. L. Wang, et al. (2004). Semiconducting and piezoelectric oxide nanostructures induced by polar surfaces. *Adv. Funct. Mater.* **14** (10), 943–956.
17. Z. L. Wang (2004). Zinc oxide nanostructures: growth, properties and applications. *J. Phys. Condens. Matter.* **16** (25), R829.
18. M. Suchea, et al. (2006). ZnO transparent thin films for gas sensor applications. *Thin Solid Films* **515** (2), 551–554.

19. W. Tress, et al. (2019). Performance of perovskite solar cells under simulated temperature-illumination real-world operating conditions. *Nat. Energy.* **4**, 568–574.
20. H.-L. Guo, et al. (2015). Oxygen deficient $ZnO_{1-x}$ nanosheets with high visible light photocatalytic activity. *Nanoscale* **7** (16), 7216–7223.
21. D. Lamas, G. Lascalea, and N. W. de Reca (1998). Synthesis and characterization of nanocrystalline powders for partially stabilized zirconia ceramics. *J. Eur. Ceram. Soc.* **18** (9), 1217–1221.
22. S. Bhaduri and S. Bhaduri (1997). Enhanced low temperature toughness of $Al_2O_3$-$ZrO_2$ nano/nano composites. *Nanostr. Mater.* **8** (6), 755–763.
23. R.-C. Wang and C.-C. Tsai (2009). Efficient synthesis of ZnO nanoparticles, nanowalls, and nanowires by thermal decomposition of zinc acetate at a low temperature. *Appl. Phys. A* **94** (2), 241–245.
24. M. Ristić, et al. (2005). Sol–gel synthesis and characterization of nanocrystalline ZnO powders. *J. Alloys Compd.* **397** (1), L1–L4.
25. Y.-H. Ni, et al. (2005). Hydrothermal preparation and optical properties of ZnO nanorods. *Mater. Sci. Eng. B* **121** (1), 42–47.
26. N. Scarisoreanu, et al. (2005). Properties of ZnO thin films prepared by radio-frequency plasma beam assisted laser ablation. *App. Sur. Sci.* **247** (1), 518–525.
27. S.-S. Chang, et al. (2002). Luminescence properties of Zn nanowires prepared by electrochemical etching. *Mater. Lett.* **53** (6), 432–436.
28. A. K. Zak, et al. (2013). Sonochemical synthesis of hierarchical ZnO nanostructures. *Ultrason. Sonochem.* **20** (1), 395–400.
29. M. Kooti and A. Naghdi Sedeh (2012). Microwave-assisted combustion synthesis of ZnO nanoparticles. *J. Chem.* **2013**, 1–4.
30. O. Singh, N. Kohli, and R. C. Singh (2013). Precursor controlled morphology of zinc oxide and its sensing behaviour. *Sens. Actuators B* **178**, 149–154.
31. A. Shetty and K. K. Nanda (2012). Synthesis of zinc oxide porous structures by anodization with water as an electrolyte. *Appl. Phys. A* **109** (1), 151–157.
32. D. Rajesh, B. V. Lakshmi, and C. Sunandana (2012). Two-step synthesis and characterization of ZnO nanoparticles. *Phys. B* **407** (23), 4537–4539.
33. A. A. Mohamed, et al. (2020). Eco-friendly mycogenic synthesis of ZnO and CuO nanoparticles for in vitro antibacterial, antibiofilm, and antifungal applications. *Biol Trace Elem Res*. https://doi.org/10.1007/s12011-020-02369-4.
34. A. A. Mohamed, et al. (2019). Fungal strain impacts the shape, bioactivity and multifunctional properties of green synthesized zinc oxide nanoparticles. *Biocatal. Agric. Biotechnol.* **19**, 101103.
35. A. Fouda, et al. (2020). Optimization of green biosynthesized visible light active CuO/ZnO nano-photocatalysts for the degradation of organic methylene blue dye. *Heliyon* **6** (9), e04896.
36. A. Fouda, et al. (2018). In-Vitro cytotoxicity, antibacterial, and UV protection properties of the biosynthesized zinc oxide nanoparticles for medical textile applications. *Microb. Pathog.* **125**, 252–261.
37. S. S. Salem and A. Fouda (2020). Green synthesis of metallic nanoparticles and their prosective biotechnological applications: an overview. *Biol. Trace Elem. Res.* **199** (1), 344–370.
38. A. Vázquez, I. A. López, and I. Gómez (2013). Growth mechanism of one-dimensional zinc sulfide nanostructures through electrophoretic deposition. *J. Mater. Sci.* **48** (6), 2701–2704.
39. S. Kang, et al. (2013). Hydrothermal conversion of lignin: a review. *Renew. Sust. Energy Rev.* **27**, 546–558.
40. D. Chen, X. Jiao, and G. Cheng (1999). Hydrothermal synthesis of zinc oxide powders with different morphologies. *Solid State Commun.* **113** (6), 363–366.
41. N. A. Shad, et al. (2019). Photocatalytic investigation of cadmium oxide nanosheets prepared by hydrothermal method. *Arab. J. Sci. Eng.* **44**, 6669–6675.
42. L. Gan, et al. (2018). The fabrication of bio-renewable and recyclable cellulose based carbon microspheres incorporated by $CoFe_2O_4$ and the photocatalytic properties. *J. Clean. Prod.* **196**, 594–603.
43. A. Geng, et al. (2018). Highly efficient visible-light photocatalyst based on cellulose derived carbon nanofiber/BiOBr composites. *Cellulose* **25** (7), 4133–4144.
44. K. Leng, et al. (2018). Construction of functional nanonetwork-structured carbon nitride with Au nanoparticle yolks for highly efficient photocatalytic applications. *Chem. Commun.* **54** (52), 7159–7162.
45. M. Li, et al. (2019). Novel Z-scheme visible-light photocatalyst based on $CoFe_2O_4$/BiOBr/graphene composites for organic dye degradation and Cr(VI) reduction. *App. Sur. Sci.* **478**, 744–753.
46. C.-T. Yang, et al. (2016). A novel heterojunction photocatalyst, $Bi_2SiO_5$/$gC_3N_4$: synthesis, characterization, photocatalytic activity, and mechanism. *RSC Adv.* **6** (47), 40664–40675.
47. M. M. Sajid, et al. (2019). Facile synthesis of Zinc vanadate Zn3 (VO4) 2 for highly efficient visible light assisted photocatalytic activity. *J. Alloys Compd.* **775**, 281–289.
48. S. Agarwal, et al. (2019). Gas sensing properties of ZnO nanostructures (flowers/rods) synthesized by hydrothermal method. *Sens. Actuators B* **292**, 24–31.
49. M. Mahendiran, et al. (2019). Structural and optical analysis of 1D zinc oxide nanoparticles synthesized via hydrothermal method. *Mater. Today: Proc.* **8**, 412–418.
50. R. Saravanan, et al. (2013). Synthesis, characterization and photocatalytic activity of novel Hg doped ZnO nanorods prepared by thermal decomposition method. *J. Mol. Liq.* **178**, 88–93.
51. T. Karnan and S. A. S. Selvakumar (2016). Biosynthesis of ZnO nanoparticles using rambutan (*Nephelium lappaceum* L.) peel extract and their photocatalytic activity on methyl orange dye. *J. Mol. Struct.* **1125**, 358–365.
52. L. Chen, et al. (2012). Flower-like $Bi_2O_2CO_3$: facile synthesis and their photocatalytic application in treatment of dye-containing wastewater. *Chem. Eng. J.* **193**, 123–130.
53. J. Kaur, S. Bansal, and S. Singhal (2013). Photocatalytic degradation of methyl orange using ZnO nanopowders synthesized via thermal decomposition of oxalate precursor method. *Phys. B* **416**, 33–38.
54. J. Iqbal, et al. (2015). Facile synthesis of Zn doped CuO hierarchical nanostructures: structural, optical and antibacterial properties. *AIP Adv.* **5** (12), 127112.
55. A. Arshad, et al. (2017). Graphene nanoplatelets induced tailoring in photocatalytic activity and antibacterial characteristics of MgO/graphene nanoplatelets nanocomposites. *J. Appl. Phys.* **121** (2), 024901.
56. R. M. Douglas, et al. (1987). Failure of effervescent zinc acetate lozenges to alter the course of upper respiratory tract infections in Australian adults. *Antimicrob. Agents Chemother.* **31** (8), 1263–1265.
57. C. W. Stratton, M. P. Weinstein, and L. B. Reller (1982). Correlation of serum bactericidal activity with antimicrobial agent level and minimal bactericidal concentration. *J. Infect. Dis.* **145** (2), 160–168.
58. O. Lupan, et al. (2007). Nanofabrication and characterization of ZnO nanorod arrays and branched microrods by aqueous solution route and rapid thermal processing. *Mater. Sci. Eng. B* **145** (1–3), 57–66.
59. S. M. Mali, et al. (2018). Ultrasensitive and bifunctional ZnO nanoplates for an oxidative electrochemical and chemical sensor of $NO_2$: implications towards environmental monitoring of the nitrite reaction. *RSC Adv.* **8** (20), 11177–11185.

60. Y. Qiu, W. Chen, and S. Yang (2010). Facile hydrothermal preparation of hierarchically assembled, porous single-crystalline ZnO nanoplates and their application in dye-sensitized solar cells. *J. Mater. Chem. A* **20** (5), 1001–1006.
61. X. Wang, et al. (2010). Mass production of micro/nanostructured porous ZnO plates and their strong structurally enhanced and selective adsorption performance for environmental remediation. *J. Mater. Chem. A* **20** (39), 8582–8590.
62. J. H. Zeng, B. B. Jin, and Y. F. Wang (2009). Facet enhanced photocatalytic effect with uniform single-crystalline zinc oxide nanodisks. *Chem. Phys. Lett.* **472** (1–3), 90–95.
63. Z. Jing and J. Zhan (2008). Fabrication and gas-sensing properties of porous ZnO nanoplates. *Adv. Mater.* **20** (23), 4547–4551.
64. C.-L. Kuo, T.-J. Kuo, and M. H. Huang (2005). Hydrothermal synthesis of ZnO microspheres and hexagonal microrods with sheetlike and platelike nanostructures. *J. Phys. Chem. B* **109** (43), 20115–20121.
65. T. Tynell and M. Karppinen (2014). Atomic layer deposition of ZnO: a review. *Semicond. Sci. Technol.* **29** (4), 043001.
66. S. C. Lyu, et al. (2002). Low temperature growth and photoluminescence of well-aligned zinc oxide nanowires. *Chem. Phys. Lett.* **363** (1–2), 134–138.
67. I. A. Abdelhafeez, et al. (2019). Green synthesis of ultrathin edge-activated foam-like carbon nitride nanosheets for enhanced photocatalytic performance under visible light irradiation. *Sustain. Energy Fuels.* **3**, 1764–1775.
68. H. Parangusan, D. Ponnamma, and M. A. A. Al-Maadeed (2019). Effect of cerium doping on the optical and photocatalytic properties of ZnO nanoflowers. *Bull. Mater. Sci.* **42** (4), 179.
69. J. E. Morales-Mendoza, et al. (2019). Structure and optical properties of ZnO and $ZnO_2$ nanoparticles. *J. Nano Res.* **56**, 49–62.
70. R. Bomila, S. Suresh, and S. Srinivasan (2019). Synthesis, characterization and comparative studies of dual doped ZnO nanoparticles for photocatalytic applications. *J. Mater. Sci.* **30** (1), 582–592.
71. P. Secrétan, et al. (2019). Imatinib: major photocatalytic degradation pathways in aqueous media and the relative toxicity of its transformation products. *Sci. Total Environ.* **655**, 547–556.
72. R. Farzana, et al. (2017). Antimicrobial behavior of zinc oxide nanoparticles and β-lactam antibiotics against pathogenic bacteria. *Arch. Clin. Microbiol.* **8** (4), 57.
73. N. Jones, et al. (2008). Antibacterial activity of ZnO nanoparticle suspensions on a broad spectrum of microorganisms. *FEMS Microbiol. Lett.* **279** (1), 71–76.
74. K. R. Raghupathi, R. T. Koodali, and A. C. Manna (2011). Size-dependent bacterial growth inhibition and mechanism of antibacterial activity of zinc oxide nanoparticles. *Langmuir* **27** (7), 4020–4028.
75. M. Li, L. Zhu, and D. Lin (2011). Toxicity of ZnO nanoparticles to *Escherichia coli*: mechanism and the influence of medium components. *Environ. Sci. Technol.* **45** (5), 1977–1983.
76. A. A. Nash, R. G. Dalziel, and J. R. Fitzgerald, *Mims' pathogenesis of infectious disease* (Academic Press, Cambridge, 2015).